

A quantitative comparison of lunar orbital neutron data

V.R. Eke

*Institute for Computational Cosmology, Department of Physics, Durham University, South Road, Durham.
DH1 3LE, UK*

v.r.eke@durham.ac.uk

L.F.A. Teodoro

*BAER, Planetary Systems Branch, Space Sciences and Astrobiology Division, MS 245-3, NASA Ames
Research Center, Moffett Field, CA 94035, USA*

D.J. Lawrence

Johns Hopkins University Applied Physics Laboratory, Laurel, MD 20723, USA

R.C. Elphic

NASA Ames Research Center, Moffett Field, CA 94035, USA

W.C. Feldman

Planetary Science Institute, 1700 East Fort Lowell, Suite 106, Tucson, AZ 85719, USA

ABSTRACT

Data from the Lunar Exploration Neutron Detector (LEND) Collimated Sensors for Epithermal Neutrons (CSETN) are used in conjunction with a model based on results from the Lunar Prospector mission to quantify the extent of the background in the LEND CSETN. A simple likelihood analysis implies that at least 90% of the lunar component of the LEND CSETN flux results from high energy epithermal neutrons passing through the walls of the collimator. Thus, the effective full-width at half-maximum of the LEND CSETN field of view is comparable with that of the omni-directional Lunar Prospector Neutron Spectrometer. The resulting map of high energy epithermal neutrons offers the opportunity to probe the hydrogen abundance at low latitudes, and provide constraints on the distribution of lunar water.

Subject headings: Moon — methods: data analysis

1. Introduction

The weathering of the lunar surface is so slow that it should provide extractable information about the history of volatile molecule transport within the inner Solar System, a subject of considerable relevance to water-based life on Earth. Samples of lunar regolith returned in the Apollo missions contained a sufficiently low abundance of water that these molecules were, until

recently, dismissed as terrestrial contamination (Epstein & Taylor 1973) and the Moon was considered to be dry. The change of paradigm has been driven by evidence that has accumulated over the past 15 years from a number of different missions and types of experiment (Lawrence 2011).

The first of this recent wave of techniques for divining for lunar water was the use of bistatic

circularly polarised radar measurements from the Clementine mission (Nozette et al. 1996). A peak at opposition in the ratio of returned same-sense to opposite sense circularly polarised flux was posited to be due to multiple scattering within a low-loss medium such as water ice. The signal correlated with Clementine being over the lunar poles, the locations of permanently shaded ‘cold traps’ in which water ice would be stable against sublimation for billions of years. Stacey et al. (1997) and Campbell et al. (1997) found that the same signal would also result from a surface that was rough on the scale of the 13cm wavelength of the radiation and that even in sunlit regions this same high circular polarisation ratio was seen. Thus it is unclear whether or not water ice deposits are the explanation for these observations. Theoretical modelling of the radar scattering process by Fa et al. (2011) suggests that this technique will struggle to detect ice mixed in with lunar regolith because of their similar relative permittivities. However, Spudis et al. (2010) argue, based upon measurements from Chandrayaan-1’s Mini-SAR experiment, that surface roughness cannot explain the signal seen from within some ‘anomalous’ polar craters where no signal is seen from the surrounding region, which might be expected to have had post-cratering roughness weathered away at a similar rate.

An important method that has provided evidence relevant to the discussion of lunar water over the last 13 years is neutron spectroscopy. It was realised 50 years ago that the neutron flux leaking from the Moon encoded information about the hydrogen content in the lunar surface (Lingenfelter et al. 1961). Free neutrons are created via interactions between incoming cosmic rays and nuclei within the top few metres of the lunar regolith. Having been knocked out of nuclei, these neutrons subsequently evolve by scattering off other nuclei until they either escape through the surface or have sufficiently little kinetic energy that they are absorbed by another nucleus. The fast neutrons (energies exceeding 0.5 MeV) predominantly lose energy through inelastic collisions that result in gamma rays being emitted from the temporarily excited nuclei that they hit. At intermediate energies ($0.3 \text{ eV} < E < 0.5 \text{ MeV}$), epithermal neutrons donate kinetic energy to their targets, which recoil following elastic collisions. As

hydrogen nuclei have a similar mass to that of the neutron, they are particularly effective at draining energy rapidly from epithermal neutrons and sending them down to thermal energies ($E < 0.3 \text{ eV}$), where they become increasingly susceptible to nuclear capture. Thus, a hydrogen rich top metre of regolith would be expected to produce a deficit in the epithermal neutron flux leaking from the lunar surface.

This first calculation of the anticipated sensitivity of orbital neutron measurements to the regolith hydrogen content was refined by Metzger & Drake (1990) and Feldman et al. (1991) with the benefit of improved knowledge of the regolith composition. These models were confronted with observational evidence when results from Lunar Prospector’s Neutron Spectrometer were produced (Feldman et al. 1998b). A convincing deficit of epithermal neutrons was detected in the vicinity of both lunar poles. However, Lunar Prospector (LP) was an omni-directional detector that accepted neutrons from all directions. Consequently, the spatial resolution of the published hydrogen maps was sufficiently poor that the question of how well these count rate dips correlated with surface features, such as craters, remained tantalisingly unanswered. Other results from LP’s Neutron and Gamma Ray Spectrometers (Lawrence et al. 1998; Feldman et al. 1998a,b; Elphic et al. 1998) provided a detailed and coherent picture of the lunar surface composition. The analysis of the full data set (Feldman et al. 2000, 2001), along with a detailed account of the data reduction process (Maurice et al. 2004) and improved modelling of both the detector response and variation with composition (Lawrence et al. 2006) provide a benchmark against which current and future experiments can be compared.

A recent development in the story of lunar water has come courtesy of measurements of the infra-red reflectance of sunlit regions of the Moon. Three different studies of the infra-red spectrum (Clark 2009; Sunshine et al. 2009; Pieters et al. 2009) found evidence for absorption by oxygen to hydrogen chemical bonds on the lunar surface. Furthermore, the depth of the absorption features appeared to vary with solar zenith angle. Such a result would imply the existence of a contribution by hydroxyl and water molecules to the dynamic, if tenuous, lunar exosphere. This idea of a lunar

water cycle had been considered by Butler (1997) and Crider & Vondrak (2000).

The most compelling evidence for the existence of lunar water came from the Lunar Crater Observation and Sensing Satellite (LCROSS), which trailed a spent Centaur rocket into a permanently shaded part of the Cabeus crater near to the lunar south pole. Nine instruments on LCROSS analysed the plume of material resulting from this impact. It was determined to have contained water molecules at 5.6 ± 2.9 per cent by mass (Colaprete et al. 2010). This uncertainty is dominated by the uncertainty in the total plume mass, and the detection of water vapour and water ice within the instrumental field of view was a much more significant 155 ± 12 kg.

Given that water does exist on the Moon, the question of how it came to be there becomes relevant. Arnold (1979) considered various potential sources: delivery by comets or meteorites, solar wind reduction of iron in the lunar regolith or degassing from the lunar interior. As a result of the slow weathering of the lunar surface, the quantity, isotopic ratios and distribution of water, both with depth and position on the surface, should still contain information about the history of water delivery to the Moon. It is thus important to make an accurate map of the distribution of lunar water in order to help disentangle the importance of the various delivery options.

With this aim in mind, there are two different approaches that have been taken to try to improve upon the original LP hydrogen distribution maps. The software route involves using image reconstruction techniques to undo the instrumental blurring by the omni-directional LP detector, whereas the hardware route is to make the detector itself collimated.

Elphic et al. (2007) introduced a pixon-based image reconstruction algorithm that extracted more information from the LP epithermal neutron data set, and Eke et al. (2009) showed that, when all permanently shaded regions at both poles were stacked together, these data statistically favoured a reconstruction where the hydrogen was concentrated into the permanently shaded regions. This result has important implications for the molecular form of the hydrogen, its method of delivery to the Moon and survival on the surface. With improved maps of the permanently shaded

polar regions from the Japanese SELENE mission (Noda et al. 2008), Teodoro et al. (2010) confirmed this earlier result and made lunar polar hydrogen maps that were given to the LCROSS team to help them decide where to crash their Centaur rocket in the search for water ice (Colaprete et al. 2010; Schultz et al. 2010).

The alternative approach, to deploy hardware that only accepts neutrons from a small fraction of 4π steradians, was taken with the Lunar Exploration Neutron Detector (LEND), described by Mitrofanov et al. (2008), on the Lunar Reconnaissance Orbiter (LRO). Blocking epithermal neutrons from other directions is a challenge best met by placing many moderating and absorbing nuclei in the way. However, the necessary requirement not to send large masses away from the Earth opposes this straightforward approach to producing a collimated neutron detector. An attempt to balance these competing constraints has been made with the 4 LEND Collimated Sensors for Epithermal Neutrons (CSETN1-CSETN4), hereafter referred to collectively as CSETN. This is one of seven instruments (Chin et al. 2007) on board the LRO mission that has, to date, been mapping the Moon since mid-2009.

There has been some disagreement in the literature concerning the sensitivity of the LEND CSETN. Lawrence et al. (2010) argue that the detected flux should contain about 0.18 collimated neutrons per second. This conclusion was arrived at following both analytical calculations, using geometrical considerations to scale the LP count rate, and Monte Carlo neutron transport modelling, which also provided an estimate of the uncollimated lunar background flux of 0.09 counts per second. These findings were based upon the not entirely specific description of the detector configuration provided by Mitrofanov et al. (2008). The estimate for the collimated neutron count rate given by Mitrofanov et al. (2008) is 0.9 counts per second. They also state that the total background from all sources should provide about 1.2 neutrons per second of background counts. More recently, using data gathered by the LEND CSETN during the first year in orbit around the Moon, Mitrofanov et al. (2010b) assert that the collimated neutron count rate is more like 1.9 neutrons per second, with 0.3 counts per second of uncollimated lunar signal and 2.8 neutrons per sec-

ond as a result of cosmic ray strikes on LRO itself. However, Lawrence et al. (2011) use the compositional variation of the high- and low-energy epithermal neutron count rates to estimate that the uncollimated lunar flux exceeds 2 counts per second, leaving very little collimated signal.

The abundance and distribution of near-surface lunar hydrogen provides a valuable constraint on models describing the delivery and survival of volatile materials over billions of years. Making accurate maps of the lunar hydrogen distribution is thus one of the foremost aims for those seeking to understand this important aspect of the history of the inner solar system. As the ability to detect small dips in epithermal neutron flux is paramount when using orbital neutron data to infer hydrogen abundances in the top ~ 1 m of lunar regolith, it is crucial to know precisely what is the signal-to-background ratio for the LEND CSETN. The most pertinent question to address is what fraction of the detected neutrons actually originate from the lunar surface in the small field of view of the collimator? The remainder of the detected neutrons would be uncollimated and originating either in the Moon or in the spacecraft itself.

The Geosciences Node of NASA’s Planetary Data System (PDS¹) is a public repository that archives and distributes digital data related to the study of the Moon, and it contains data from the LEND CSETN. It is thus timely to compare these new data with those collected over a decade ago by the LP Neutron Spectrometer. The count rate variation with spacecraft position and altitude provides a direct means to decompose the total detected flux into collimated signal and uncollimated background noise. The main purpose of this paper is to answer the question, what fraction of the LEND CSETN counts are epithermal neutrons that truly originate from the small piece of lunar surface geometrically accessible to the collimator?

Section 2 of this paper provides a description of the data that will be used in this study and the likelihood analysis that is employed to determine what fraction of the LEND CSETN count rate is collimated epithermal neutrons. Section 3 contains the results of using the data to decompose the total counts into those from the various com-

ponents, as well as a discussion of how robust these findings are to potential shortcomings in the modelling of the count rate. These results are compared with the component fractions advocated by Mitrofanov et al. (2010b). The findings are summarised in Section 4.

2. Method

This section contains a detailed description of the data being used, the model that is employed to describe them, and the procedure used to find the best-fitting model parameters. These parameters are the fraction of the total LEND CSETN counts coming from each of the different possible sources, namely collimated lunar neutrons, uncollimated lunar neutrons that have enough energy to pass through the sides of the collimator and uncollimated spacecraft neutrons.

2.1. Data

The data analysed in this paper are the first 15 months of ‘rectified science data’ available within the LEND Reduced Data Record (RDR) data product available at the Geosciences Node of NASA’s PDS. Data from all 4 LEND CSETN detectors are studied. The neutron count rate comprises the sum of counts in channels 10-16, because these channels mostly contain neutron detections rather than the gamma rays or charged particles that prevail in channels 1-9 (Mitrofanov, private communication). To avoid needing to know detailed information concerning neutron transport within LRO and LEND, only the observations for which the nadir angle is less than 5° are used. In this configuration, the LEND instrument lies slightly beneath and to one side of the LRO spacecraft and has an unobstructed view of the lunar surface. Other than on the first day of collection of these data (15th September, 2009), LRO was in a reasonably circular mapping orbit with altitudes generally between 40 km and 60 km. During the initial day of data, the spacecraft had yet to be put into its mapping orbit, so reached altitudes as low as 30 km and as high as 210 km. Throughout the rest of this paper, the zero of time will be defined as the start of the data collection period.

¹<http://pds-geosciences.wustl.edu>

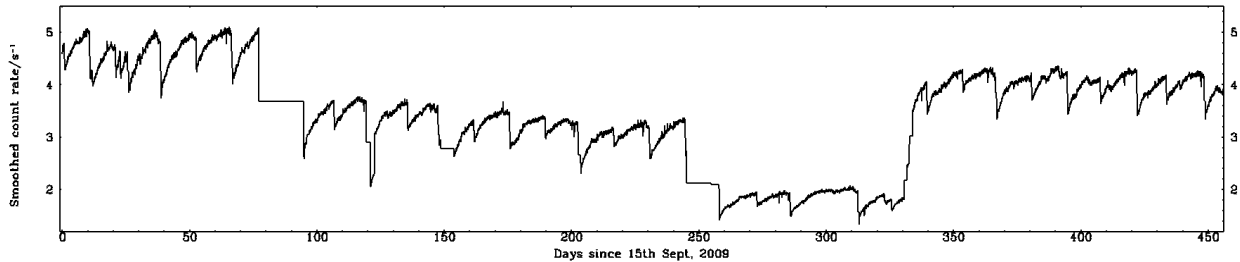


Fig. 1.— The box-car smoothed (with a box containing 10000 consecutive 1 second observations) LEND CSETN data for the first 15 months of operation.

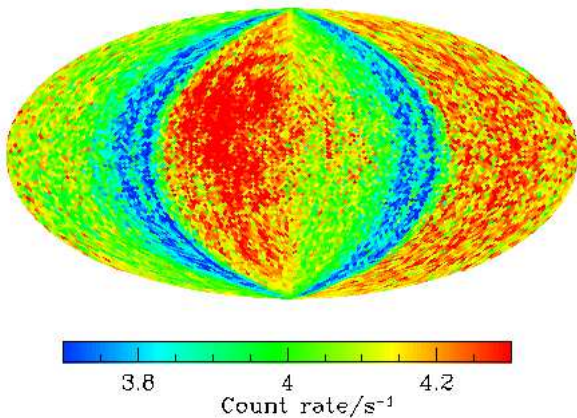


Fig. 2.— A Mollweide projection of the raw LEND CSETN channel 10-16 data. This uses the HEALPix pixellation (Gorski et al. 2005) at a resolution of $N_{\text{side}} = 64$, which corresponds to a pixel side length of ~ 28 km.

2.1.1. Long-term temporal variations in the time series data

The box-car smoothed time series data are shown in Fig. 1. It is apparent that there are some glitches in these smoothed count rates. These are almost always associated with periods when no data are available from the detectors, and have a periodicity of roughly 2 weeks, or approximately half a lunar month. After the glitches, the count rate can be as much as 20% lower than before, and it gradually rises over a period as long as a few weeks. Fig.2 shows a map of the raw count rate. It is apparent that there are bands of low counts at $-110^\circ < \text{longitude} < -90^\circ$ and $70^\circ < \text{longitude} < 90^\circ$, and bands of high count rate at $-80^\circ < \text{longitude} < -0^\circ$ and $100^\circ < \text{longitude} < 180^\circ$. The detectors are orbiting in a plane whose normal is approximately the Earth-Moon axis when they are switched off.

These artefacts are largely removed when the temporal variability is modelled as described in the next section. Recorded count rates are sometimes unusually high both slightly before and after the glitch times, so data are removed in the periods 5 minutes prior to the time when the data stop and 1 minute after the time when they reappear.

The one example of a glitch where the count rate jumps upwards is found at $t \sim 122.5$ days, within a short period between two other glitches. To avoid any problems this might introduce, all data with $[120 < t/\text{days} < 123]$ are discarded.

Other notable features of Fig. 1 are that there are gaps without data at $t \sim 80$ and 250 days, after which the flux is significantly lower. As described on the PDS, this is because CSETN3 and

CSETN2 respectively are switched off at these times. Both of these detectors recommence recording data around $t \sim 335$ days. Along with the temporal variation described above, this should also be accounted for when trying to predict the total counts for any particular observation.

The number of 1s observations remaining after pruning the data as described above is ~ 35 million. They span a total of 456 days from 15th September, 2009. Various subsets of these data are used in Section 3 to investigate the robustness of the results, but the default in this paper is to use all of these observations.

2.2. Model

There are 3 components that will contribute to the LEND CSETN channel 10-16 count rate. The magnitudes of each component will depend upon a combination of the spacecraft latitude, longitude and altitude, a . The components are:

- 1) collimated lunar epithermal neutrons,
- 2) uncollimated lunar neutrons, with energies high enough to make it through the walls of the collimator,
- 3) spacecraft-derived neutrons also entering into the detectors.

The final component may also include any contribution to the channel 10-16 count rate due to charged particles resulting from cosmic rays striking the spacecraft.

The ^3He tubes used to count incoming neutrons in LEND, and also LP, are covered in cadmium to keep out low energy, thermal neutrons at energies below $\sim 0.4\text{eV}$. The energy dependence of both the detector efficiency (Lawrence et al. 2002) and the lunar neutron leakage flux (McKinney et al. 2006) means that low energy epithermal (LEE) neutrons with $\sim 0.4 - 100\text{eV}$ provide the bulk of the counts in these detectors. In addition to the Cd coating, the LEND CSETN are placed inside a collimator that consists of layers of polyethylene to moderate the neutrons and ^{10}B to absorb the moderated neutrons. Lawrence et al. (2011) estimate that the collimator is largely transparent for neutrons that strike it with at least $\sim 10\text{keV}$. Incident neutrons at these higher energies could be moderated to a low enough energy that the ^3He counter is able to detect them. It is this route

that neutrons comprising components (2) and (3) must take in order to contribute to the LEND CSETN count rate. Component (2) reflects the high energy epithermal (HEE) neutron flux from the lunar surface; an interesting science product in itself.

The technique employed here essentially constructs a model for the total count rate that the LEND CSETN should measure in each 1s observation from each of the components. This model is based upon the LP maps of fast, moderated, epithermal and thermal neutron flux and a spatially invariant spacecraft background. Each of the model component fluxes also requires the inclusion of both an altitude dependence and the temporal count rate gain variation, $g(t)$. Once the individual components have their latitude, longitude, altitude and time variations computed, they are each normalised such that a fraction f_i of the total counts summed over all observations in the data set comes from component i . In this nomenclature, determining f_i is the purpose of this paper. The LEND CSETN data are used to determine the relative probabilities of the different sets of component fractions, f_i , i.e. they determine which component fractions provide the best match to the time series measurements.

The evaluation of the spatial, altitude and temporal variations of the model component fluxes are described in the following subsections.

2.2.1. Constructing the spatial variation in the model

Given the well documented and well understood LP maps for the spatial variation of the thermal, epithermal and fast neutron fluxes, these data sets are the natural resource for designing whole-Moon templates of the various components of the LEND CSETN flux. Each component of the model requires a template that describes how the relative count rate varies with longitude and latitude. These templates will hereafter be denoted with u_i for component i , and their normalisation is discussed at the end of subsection 2.2. To model the spatial variation of the components of lunar origin, various different resolution maps of the LP neutron data are made using the HEALPix pixelation scheme (Gorski et al. 2005). This partitioning of the sphere has 12 equal area base pixels and finer pixelations are achieved by splitting each of

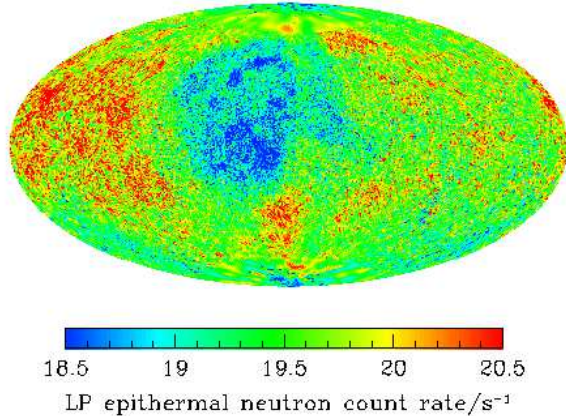


Fig. 3.— A Mollweide projection of the LP epithermal neutron map including the pixion reconstructions in the polar regions, which is used as the template for component (1) of the model. This uses the HEALPix pixellation at a resolution of $N_{\text{side}} = 64$, which corresponds to a pixel side length of ~ 28 km.

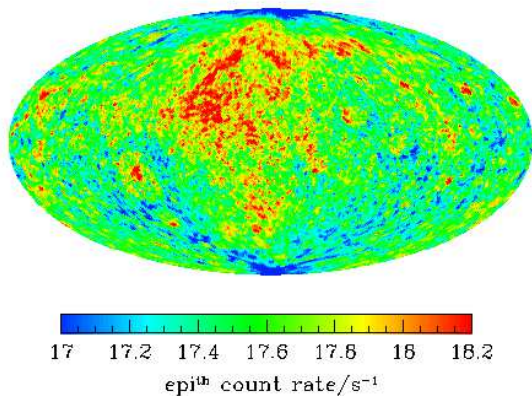


Fig. 4.— A Mollweide projection of the thorium-corrected epi^{tho} map, used as part of component (2) in the model. This uses the HEALPix pixellation at a resolution of $N_{\text{side}} = 64$.

the pixels into 4 equal area pixels. The level of resolution can be denoted by N_{side} , the number of pixels along a side of a base pixel. In this nomenclature, the total number of pixels describing the spherical surface is $N_{\text{pix}} = 12N_{\text{side}}^2$ and, for the Moon, the typical pixel side length for the k th level of refinement is $l_k = (1778/N_{\text{side}})$ km.

Given that LRO can be at altitudes from 30 – 210 km, although it spends most of the time at its nominal mapping altitude of 50 km, it is necessary to choose the appropriate resolution template, when calculating the model counts for a particular observation. This is done quite crudely by linearly interpolating between the pixel values either side of the FWHM for the component under consideration. There are inevitable inaccuracies in this treatment, both because LP did not have comparable spatial resolution to component (1), and it did not produce a HEE map containing the same spectrum of neutron energies as would be expected to produce component (2). However, this simple approach will still provide an adequate comparison between LP and LEND CSETN data sets.

It is necessary to find an expression for the variation of the FWHM with altitude, so that an appropriate pixellation can be chosen to give a suitably smoothed measure of the lunar flux. This can be achieved by considering the neutron flux emanating from a small area on the lunar surface. If the detector is orbiting at an altitude a , a distance r from the neutron source under consideration, with a corresponding arc length s between the sub-spacecraft point and the source, then the relative flux received can be written as

$$\frac{f(s)}{f(s=0)} = \left(\frac{a}{r}\right)^2 (\cos\theta)^{1+\alpha}, \quad (1)$$

where α represents the effective beaming of neutrons relative to the constant surface brightness, Lambertian case, and θ is the angle from the surface normal to the spacecraft. This ‘beaming’ arises because the epithermal neutron number density increases with depth in the top layer of the regolith (McKinney et al. 2006), and is analogous to solar limb darkening. Using Monte Carlo neutron transport models, Lawrence et al. (2006) found that $\alpha \sim 0.5$ provided a good description of the beaming of epithermal neutrons from the lunar surface. Simple trigonometry yields the fol-

lowing expression for the change in flux with sub-spacecraft distance along the surface, from which the altitude dependence of the FWHM can be calculated:

$$\frac{f(s)}{f(s=0)} = \left(\frac{a}{r_M}\right)^2 \frac{[y \cos(s/r_M) - 1]^{1+\alpha}}{[y^2 + 1 - 2y \cos(s/r_M)]^{\frac{3+\alpha}{2}}}, \quad (2)$$

where $r_M = 1737.4$ km represents the lunar radius and $y = (r_M + a)/r_M$. This expression assumes that the detector has no preferred direction. While not strictly true, comparison of the inferred LP point-spread function (PSF) with that of Maurice et al. (2004) suggests that it is an adequate description in that case.

Having described how the component templates will be used, the next step involves actually creating them. The template for the collimated LEE component should look like a noiseless, high spatial resolution version of the LP epithermal neutron map. While the spatial resolution of the LP epithermal map is that of an omni-directional detector, in the polar regions, the pixon reconstructions of the LP epithermal data (Teodoro et al. 2010) can be used to gain higher spatial resolution for the LEE component (1) template, u_1 , as shown in Fig. 3. Using the pixon maps allows the model to be extended from a resolution of $N_{\text{side}} = 64$ to $N_{\text{side}} = 128$ and 256 at $|\text{lat}| > 71^\circ$. This highest resolution roughly corresponds to the anticipated footprint for component (1) in the model. The results do not depend greatly on this detail in the model, as demonstrated in Section 3.

The spatial variation of the HEE component (2) is somewhat less easy to estimate, both because the relevant incident neutron energies depend upon precise details of the collimator, which are not available, and there does not exist a high-fidelity map of lunar neutron emission integrated with the appropriate energy-dependent filter. However, neutron data from the LP Gamma-ray Spectrometer (GRS) anticoincidence shield (Genetay et al. 2003) were used to derive information from epithermal neutrons in the energy range $100 - 500$ keV, which has significant overlap with the LEND HEE neutrons. These ‘moderated’ neutrons showed a strong correlation with LP-measured fast neutrons (Maurice et al. 2000), which themselves are correlated with average atomic mass (Gasnault et al. 2001). The mea-

sured correlation of moderated neutrons with fast neutrons suggests that the HEE neutrons may also, in part, be correlated with fast neutrons. The LP moderated neutron data are consistent with neutron transport models that show HEE neutrons are highly correlated with fast neutrons and average atomic mass (Lawrence et al. 2011) in regions with low concentrations of hydrogen. For regions with enhanced hydrogen concentrations, modelled HEE neutrons (Lawrence et al. 2011) and measured moderated neutrons (Genetay et al. 2003) show a decrease in neutron count rates that is very similar to LEE neutrons.

Based on this information, a variety of educated guesses can be made for a HEE template by considering all of the LP thermal, epithermal, moderated and fast neutron maps. In this study, two different types of initial HEE template have been devised. For the first template, a map similar to the epi* constructed by Feldman et al. (1998b) is created by subtracting 6.4% of the LP thermal count rate from the LP epithermal map, which effectively removes the LEE compositional variation due to neutron absorption at energies below 100 eV. To account for a fast neutron contribution as described above, a to-be-determined amount of the LP fast neutron map is added. The precise fraction of fast neutrons depends on details of the LEND construction, and is therefore left for the data to select.

An option of correcting for residual, nearside neutron absorption in the epi* map is also considered by subtracting a portion of the LP thorium concentrations (Lawrence et al. 2003) that spatially correlate with the residual neutron absorptions. Fig. 4 shows the template for this epi^{tho} component of the HEE variation and Fig. 5 shows the LP fast neutron map, which also contributes to u_2 , the template for component (2).

The second method involves replacing all regions of the LP epithermal map where the LP thermal counts are lower than 20 neutrons per second with a scaled version of the LP fast neutron map. This is essentially targetting the mare regions, where the LEE and thermal neutrons have a dip in count rate, whereas the fast neutrons have an excess as would be expected from LP moderated neutron measurements and HEE neutron transport simulations. Unlike for component (1), the HEE lunar template only needs to be con-

structured at the low resolution corresponding to an uncollimated detector.

By using only nadir facing observations, the spacecraft background should be independent of location over the surface, although not independent of altitude, so u_3 is taken to be a constant, independent of latitude and longitude.

2.2.2. Constructing the altitude dependence in the model

The altitude dependence of the lunar flux components, h_1 and h_2 , can be found by integrating eq. (2) over the appropriate fraction of the lunar surface out to the horizon for the chosen altitude, a . For the collimated epithermal component, the limit of the integration surface is approximated as $s = a\beta_{\text{col}}$, where $\beta_{\text{col}} = 5.6^\circ$ is the half-opening angle of the collimator. There is almost no altitude variation of the collimated component because the flux from each visible patch of surface drops like a^{-2} , while the area of surface grows like a^2 . As the beaming of neutrons is weak, the Moon presents a disc of almost uniform neutron surface brightness, these two factors almost entirely cancel out, provided that the Moon always fills the collimator's field of view.

The uncollimated lunar HEE component is computed in a similar way by integrating out to the horizon. In this case, as the spacecraft altitude increases, the Moon subtends a smaller angle and the uncollimated flux decreases. One might expect that the beaming of HEE would differ from that of LEE, because HEE neutrons are more likely to have been created by cosmic rays hitting the lunar surface at more grazing angles. The model is given the freedom to choose a value of $\alpha \neq 0.5$ for component (2), if the data prefer.

The altitude dependence of the spacecraft flux arises as a result of the solid angle of cosmic ray-containing sky blocked out by the Moon. Consequently, higher altitudes lead to more cosmic rays hitting the spacecraft and more locally generated neutrons being detected by the LEND CSETN. The flux of cosmic rays hitting the spacecraft as a whole varies like

$$\text{CRF} \propto \left(1 + \sqrt{1 - \frac{1}{y^2}}\right). \quad (3)$$

One might wonder if the flux of cosmic rays hitting the nadir facing side of LRO is more relevant for

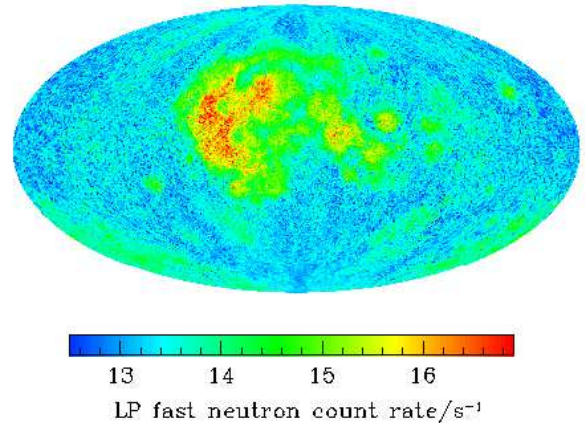


Fig. 5.— A Mollweide projection of the LP fast neutron map, used as part of component (2) in the model. This uses the HEALPix pixellation at a resolution of $N_{\text{side}} = 64$.

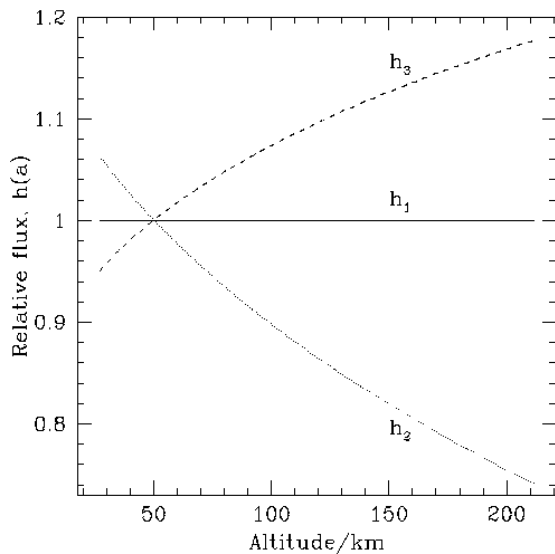


Fig. 6.— The altitude dependence, $h(a)$, of the count rates for the various different components. A solid line traces the variation with altitude of the collimated LEE lunar flux. Uncollimated HEE lunar flux, h_2 , drops off as shown by the dotted line. The spacecraft flux, h_3 , is traced by the dashed line.

predicting the neutron flux reaching LEND. This varies with altitude more rapidly:

$$\text{CRF} \propto \sqrt{1 - \frac{1}{y^2}}. \quad (4)$$

An experiment was performed where two components of uniform background were introduced, one with no altitude dependence and another varying like eq. (4), these being the extreme limits of how component (3) might depend upon altitude. The data picked out a most likely model with a combination of these two components that corresponded to an overall spacecraft background altitude dependence as given by eq. (3). Thus, the altitude dependence of component (3) was set to

$$h_3 \propto \left(1 + \sqrt{1 - \frac{1}{y^2}}\right). \quad (5)$$

Fig.6 shows the altitude dependence of all three model components of the count rate, with each normalised to unity at $a = 50$ km.

2.2.3. Constructing the temporal variation in the model

The variation of the effective count rate gain of the detector must be accounted for in the model to describe the received flux as a function of longitude, latitude, altitude and time. While the reason for the glitches and gradual recoveries in the count rate is unclear, physical systems might be expected to have exponentially time-varying behaviour. Thus, a natural and effective function to fit to each interglitch period is

$$C = C_0 + A(1 - e^{-\lambda(t-t_0)}), \quad (6)$$

where C represents the count rate, t , the time, C_0 is the count rate at a reference time t_0 in this interglitch period, and A and λ are constants to be determined by fitting to the data. This approximate correction is applied for the first evaluation of the most likely component fractions. It takes into account the exponential recoveries in count rate and the sharp drops across periods when the detectors are not returning measurements. If there are any cosmic ray flux variations on timescales of a week or longer, then they will also be absorbed into this empirical temporal correction.

Any temporally correlated residual differences, on timescales shorter than about a week, between

the most likely model and the data are assumed to result from cosmic ray flux variations. These are estimated using the boxcar smoothed data and model over periods of 40ks, and this ‘cosmic ray’ factor can also be placed into the temporal variation in the model. It is, of course, possible that inexact glitch removal can lead to incorrectly inferred cosmic ray variation, as these two factors are essentially degenerate. Only the assumption that the glitches are described by eq. (6) decouples the two. Mitrofanov et al. (2010b) do not mention the glitches in the data despite the fact that they require systematic corrections more than an order of magnitude greater than the quoted statistical uncertainties in their results. A comparison of the inferred relative cosmic ray flux with an independent proxy, namely the terrestrial neutron flux, is given in Section 3.

To take into account the combination of the long-term variations in the data, count rates for each model component are normalised to produce the observed total number of counts over the entire data set when $f_i = 1$. This corresponds to 3.58 counts/second. As a result, each observation time has its own normalisation factor, defined such that the measured count rate is a factor $g(t)$ times what it would have been without these temporal variations associated with the detectors. For the initial likelihood evaluation, $g(t)$ only corrects for the varying number of detectors and the glitches in the data, whereas for the second likelihood evaluation it also includes the cosmic ray correction factor.

Taking into account all of these different components of the modelled count rate, the anticipated count rate for any given observation, j , can be written as

$$m_j = g(t_j) \sum_{i=1}^3 f_i h_i(a_j) u_i(t_j). \quad (7)$$

The free parameters are the component fractions, f_i , determining the relative contributions of the components. In fact only 2 of these are independent because the sum of all fractions is 1 in order to recover the correct mean neutron count rate.

2.3. Likelihood evaluation

By choosing a particular set of fractions, $\{f_i\}$, it is possible to determine what is the probability of

measuring the time series LEND CSETN data set. Varying $\{f_i\}$ allows the most likely set of component fractions to be inferred. The probability of measuring d_j counts in observation j , where the model predicts m_j counts, is given by the Poisson distribution:

$$P_j = \frac{m_j^{d_j} e^{-m_j}}{d_j!}. \quad (8)$$

If the likelihood of measuring a set of n_{obs} data values is denoted by

$$L = \prod_{j=1}^{n_{\text{obs}}} P_j, \quad (9)$$

then, ignoring the model-independent denominator, a log-likelihood can be defined as

$$\ln L = \sum_{j=1}^{n_{\text{obs}}} (d_j \ln(m_j) - m_j). \quad (10)$$

The log-likelihood is calculated throughout the relevant region of the component fraction hyper-space, and the most likely parameter values, as defined by the data, are located. These log-likelihoods can be converted back to probabilities that the LEND CSETN data would arise given this model, and normalised so that the probability integrated over parameter space equals 1. The one-dimensional marginalised probability can be calculated by integrating these probabilities at fixed values of any particular parameter, f_i . An additional constraint is that none of the components is allowed to produce a negative contribution to the count rate.

3. Results

This section contains the results of applying the method described in Section 2 to the LEND CSETN data. Before describing the inferred component fractions, two additional improvements to the previously outlined model are described. These are essentially motivated by information in the data themselves.

3.1. Additional empirical corrections

Using the HEE template based upon the combination of the thermal-corrected LP epithermal and LP fast neutron maps, the entire 15 months

of glitch-corrected LEND CSETN were used to determine the maximum likelihood component fractions. The temporal correlations in the residuals between the data and most likely model, on time scales of 40ks, are assumed to arise as a result of variations in the cosmic ray flux. This implies that, with the residual for each time series measurement defined as

$$R_j = d_j - m_j, \quad (11)$$

periods when the residuals are systematically positive or negative correspond to times when the cosmic ray flux is high or low respectively.

A test of this assumption is shown in Fig. 7 with the correlation of the ratio of the smoothed LEND CSETN data to the smoothed model values and the neutron flux measured on Earth at the Thule station operated by the Bartol Research Institute. It is apparent in the time series in Fig. 7 that high neutron fluxes are often coincident with periods where the LEND CSETN data are systematically higher than the most likely model predicts. Considering the ratio of smoothed data to smoothed model as a proxy for cosmic ray flux, the relative mean values for each day can be compared with the ground-based data. A straightforward test gives a Spearman rank correlation coefficient of 0.19, which is highly significant.

Fig. 7 also shows a long-term trend in the Thule data that is not present in the LEND CSETN cosmic ray proxy. This is because that temporal variation has been absorbed into the glitch correction described earlier. Consequently, a fairer comparison results from normalising the ground-based count rates by their one-month box-car smoothed values. This effectively removes the long timescale trends from the Thule data. In this case, the comparison between the LEND CSETN cosmic ray proxy and the detrended Thule neutron count rate gives a Spearman coefficient of 0.38. A comparable test for data from other monitoring stations gives Spearman coefficients of 0.32 (Swarthmore/Newark), 0.29 (McMurdo) and 0.27 (South Pole), all of which are highly statistically significant.

This evidence provides an important consistency check for the model used here - namely that one can infer something like the cosmic ray flux from just the LEND CSETN count rates and the approximate glitch corrections represented by

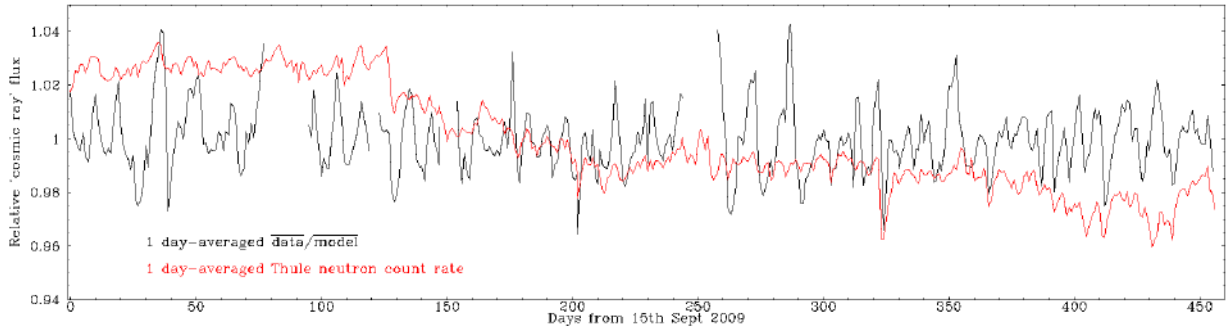


Fig. 7.— Time series showing the variability in the 1-day averaged neutron flux at the Thule station of the Bartol Research Institute and the ratio of the 40ks box-car smoothed LEND CSETN data to the similarly smoothed model. Both of these quantities can be viewed as proxies for the variability in the cosmic ray flux.

eq. (6). Using the temporal correlations in the ratio of smoothed data to smoothed model on scales of 40ks as a proxy for the variability of the cosmic ray flux, the correction factor, $g(t_j)$, is multiplied by this cosmic ray correction factor to remove these correlated residuals, and the maximum likelihood component fractions are recalculated.

This second iteration makes very little difference to the inferred component fractions, although it does significantly improve the match of the most likely model to the time series data. A map of the residuals from this second iteration is shown in Fig. 8. The pixel size is ~ 220 km, corresponding to $N_{\text{side}} = 8$ in the HEALPix notation. While the temporal correlations in the residuals have been removed, there are still significant spatially correlated residuals. The collimated flux should have a spatial dependence that is well described by component (1) in the model, but, as noted in Section 2, the HEE component is more of a challenge. The most likely reason for these residuals is an inappropriate choice of model HEE template, so it is updated to remove all of the residuals measured on the large scales shown in Fig. 8. The largest correction factor in the template count rate arising from this change is only $\sim 3\%$. While this decreases the number of degrees of freedom provided by the data, it does not preclude the residuals on smaller scales subsequently being used to test how well the model describes the data.

In contrast to the temporal correction, which could be cross-checked against an independent estimate of the cosmic ray flux, there is no other available map of the Moon with the appropri-

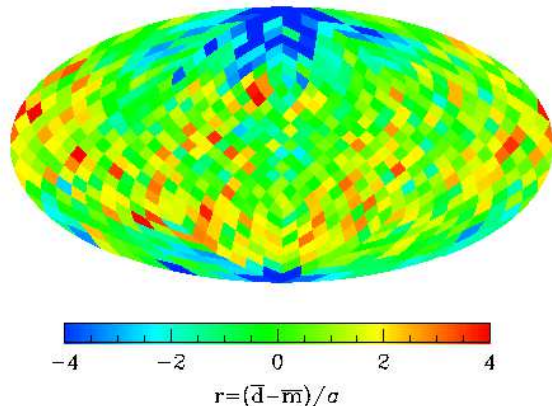


Fig. 8.— The spatial correlation of the reduced residuals (residuals normalised by an uncertainty in the pixel, σ , derived from Poisson counting statistics) for the default HEE template, having only corrected for the cosmic ray flux variations. Blue regions represent areas where the model overestimates the LEND CSETN data. $N_{\text{side}} = 8$ is used for this map, corresponding to pixel scales of ~ 220 km.

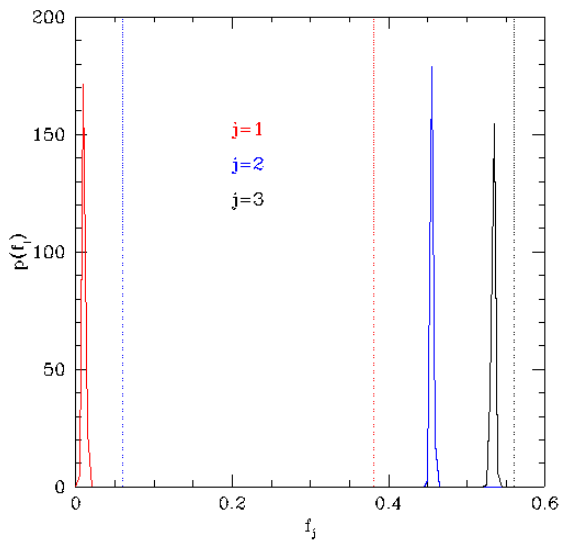


Fig. 9.— Marginalised probability distributions for the fractions of the total LEND CSETN counts in components: 1 - collimated lunar LEE neutrons (red), 2 - uncollimated lunar HEE neutrons (blue), and 3 - locally produced spacecraft neutrons (black). The coloured vertical dotted lines are the corresponding values asserted by Mitrofanov et al. (2010b).

ate energy-dependent filter applied, whatever that might be in detail. One reason to think that this is not greatly biasing the results of this study is that, when starting from the alternative HEE template described in the previous section, the residuals are significantly improved relative to those in Fig. 8 and despite this, the inferred component fractions hardly change. Thus the results found here are robust to choosing very different input HEE templates.

3.2. Most likely component fractions

Fig. 9 shows the marginalised 1D probability distributions for the component fractions after both the cosmic ray correction and the HEE map modification. The most likely component fractions only change from $\{f_1, f_2, f_3\} = \{0.02, 0.44, 0.54\}$ to $\{0.01, 0.445, 0.535\}$ as a result of both of these changes. Statistical uncertainties on these values, as represented by the widths of the probability distributions are barely more than ~ 0.01 . There are larger systematic uncertainties that are considered in more detail later in this section. The preferred component fractions reported by Mitrofanov et al. (2010b) are also shown in this figure. Including the range of values they quote, their f_3 is consistent with that found here, namely just over half of the LEND CSETN count rate comes from neutrons originating in the spacecraft itself. However, the division of the lunar flux between components (1) and (2) is effectively reversed, with Mitrofanov et al. (2010b) claiming that the collimated flux forms the vast majority, whereas the LEND CSETN data, coupled with the simple model based on previous knowledge from LP presented in this paper, suggests that the lunar flux has roughly ten times as much coming through the collimator walls in a dominant component (2) as it does in collimated neutrons.

One might wonder if the reason for this discrepancy is that the LEND CSETN detector itself perhaps has a very different behaviour to the LP epithermal neutron detector, despite the fact that they are both ^3He -filled Cd-covered tubes. If this were the case, then the model for component (1) could be in error, leading to incorrect component fractions. However, if one considers the map of lunar neutrons produced by the LEND SETN, which is an equivalent detector strapped to the outside of the LEND collimator, this expla-

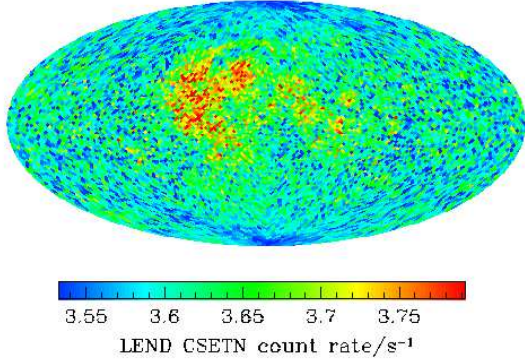


Fig. 10.— Mollweide projection of the LEND CSETN corrected count rate map, using $N_{\text{side}} = 32$, which corresponds to a pixel side length of ~ 56 km.

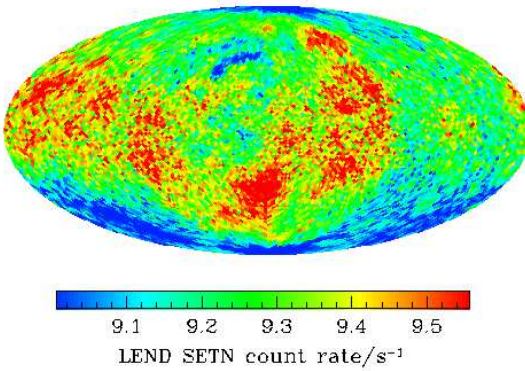


Fig. 11.— Mollweide projection of the LEND SETN corrected count rate map, using $N_{\text{side}} = 32$.

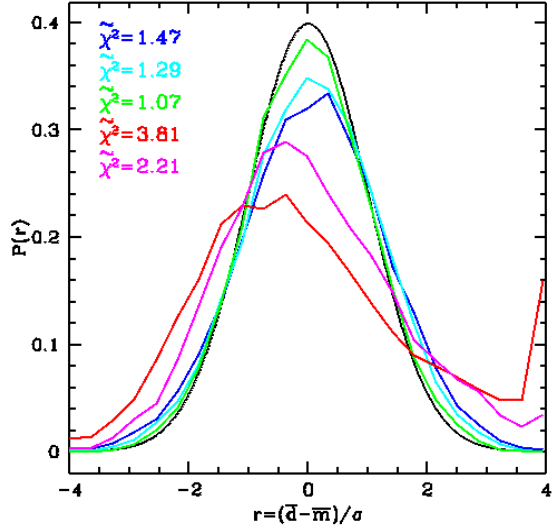


Fig. 12.— Histograms of the reduced residuals, r , in pixels at a resolution of $N_{\text{side}} = 32$. The black curve is a Gaussian with width 1. Blue, cyan and green curves show the results for the most likely model before any corrections, after the cosmic ray correction, and after both cosmic ray and HEE template corrections respectively. The reduced χ^2 values, accounting for the decrease in the number of degrees of freedom caused by the data-based corrections, are given in corresponding colours in the legend. Results in red and magenta are for the component fractions favoured by Mitrofanov et al. (2010b) and Mitrofanov et al. (2011) respectively.

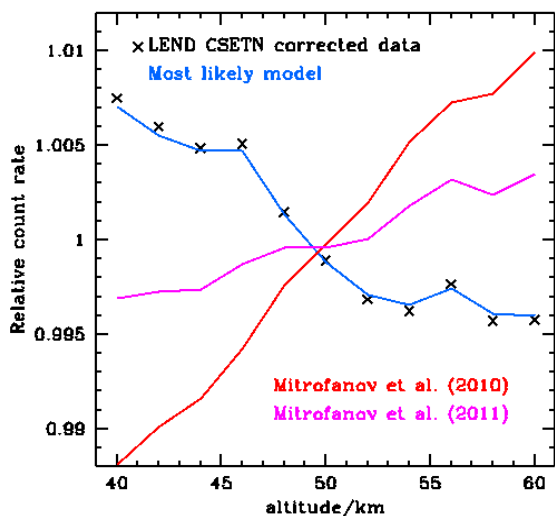


Fig. 13.— The relative count rate as a function of altitude. Points show the corrected LEND CSETN data (uncertainties are smaller than the symbol size). The blue, red and magenta lines show the trends from the most likely model found here and the asserted component fractions of Mitrofanov et al. (2010b) and Mitrofanov et al. (2011) respectively.

nation can be rejected. Figures 10 and 11 show the corrected (for glitches and cosmic ray variations) maps for the LEND CSETN and SETN respectively. It is clear from this comparison that the CSETN map is not a sharp version of that from the SETN, which is what would be produced if the lunar variability in the CSETN map were dominated by collimated neutrons. The lunar dependence of the CSETN map is driven by something different to the SETN results. This is not consistent with the asserted component fractions of Mitrofanov et al. (2010b). Instead it reflects the preponderance of higher energy neutrons in the CSETN lunar flux. In fact, Mitrofanov et al. (2011) state that a significant fraction of their ‘local background from the LRO spacecraft’ is actually scattered lunar HEE, which will have both a different spatial and altitude dependence to background arising from cosmic rays striking LRO. They give $\{f_1, f_2, f_3\} = \{0.32, 0.22, 0.46\}$ as the component fractions.

One can study the distribution of pixel reduced residuals, r , (i.e. residuals normalised by the Poisson counting error in each pixel) on scales smaller than that used for updating the HEE model template to see how well the most likely models fit the LEND data. Fig. 12 shows histograms of the pixel residuals for $N_{\text{side}} = 32$ for the most likely models before either cosmic ray or HEE template corrections, after each of these model updates, and for both the Mitrofanov et al. (2010b) and Mitrofanov et al. (2011) component fractions fed into this corrected model. The most likely model improves significantly as a result of the temporal and spatial corrections. However, even before either of them, it was still vastly superior to either the component fractions of Mitrofanov et al. (2010b) or Mitrofanov et al. (2011), for which the jump in the distribution at $r = 4$ contains all pixels with residuals at least this large. These are essentially pixels in the mare regions where the data show a high count rate while the collimated flux should show a decrease relative to other equatorial locations. The number of degrees of freedom is such that, for a good fit, the reduced χ^2 should be 1 ± 0.01 . Thus, even after both corrections, the most likely model found here is still not quite a ‘good’ fit. However, given the approximate treatment of the spatial component of the modelling on scales of the instrumental PSF, this is an im-

pressive agreement considering the small number of model parameters being fitted to the data.

Given the significant difference between the most likely component fractions found here, and those advocated by Mitrofanov et al. (2010b) and Mitrofanov et al. (2011), one might expect that there would be other tests that would allow the data to choose between these two models. In particular, given that the uncollimated lunar flux decreases strongly with increasing detector altitude, whereas the collimated flux is approximately constant, the altitude dependence of the data should also be a powerful discriminant. There are correlations of typical spacecraft altitude with position over the surface, such that LRO is usually lower over the mare regions than elsewhere, so one needs to account for these by comparing each time series observation with the model count rate for that observation. These results, normalised by the mean overall count rate and binned with respect to altitude, are shown in Fig. 13. The data show a slight decrease of count rate with increasing altitude that can only be reproduced if the model contains enough uncollimated lunar flux to overcome the opposite trend brought from the dominant spacecraft background (see Fig. 6). Once again, the asserted component fractions of both Mitrofanov et al. (2010b) and Mitrofanov et al. (2011) are completely inconsistent with the data. They imply an altitude dependence that is the opposite of that seen in the data. This points to the lunar flux predominantly being uncollimated rather than collimated.

3.3. Investigation of potential systematic errors

Given that the statistical uncertainties are so small, it is pertinent to ask how sensitive are these results to different assumptions underpinning the model. Table 1 contains results for various different model assumptions and subsets of the data, from which it is possible to gain some insight into the robustness of the inferred component fractions.

The effect of not correcting the HEE template using the residuals is shown in row 2, whereas neglecting the ‘cosmic ray’ temporal correction too leads to the fractions in row 3. While these corrections greatly improve the residuals, as shown in Fig. 12, they have no significant impact on the most likely component fractions. Rows 4 and

5 show the inferred most likely component fractions for the cases where the initial HEE template does not include the thorium correction and for the alternative LP epi/fast template respectively. Once again, the component fractions are robust to these changes to the model. The same story is repeated for rows 6 and 7, where the decoupled pixon reconstructions of the LP epithermal map reported in Teodoro et al. (2010) are replaced with the coupled ones produced by Eke et al. (2009), or just the straightforward binned LP data. The final aspect of the model that was varied was the minimum pixel size used to bin the LP data to make the templates for the HEE model. Rather than using the default $N_{\text{side}} = 64$, one tier higher HEALPix resolution was adopted to model the HEE component. Once again, this made little difference, despite gaining some resolution at the cost of introducing more noise in the model template for the HEE component. Changing the pixel size for the LEE component also had little effect, because it is such a sub-dominant component.

These results all provide evidence to support that none of the more uncertain aspects of the model are greatly impacting upon the component fractions inferred here. Keeping the default model choices, the data themselves were then split into different subsets, to see if similar results were obtained.

Splitting the time series data into the 4 distinct periods within which the number of active collimators does not change yields the results in rows 9-12. There seems to be a slight preference for data taken after $t = 90$ days to have a higher fraction in the collimated component, mostly at the expense of the spacecraft background. It is difficult to ascertain what aspect of the experiment altered to give rise to this change, which is statistically significant.

Restricting the data to include only observations made from restricted ranges in altitude does not appear to make any strong systematic changes to the inferred component fractions (rows 13-15). Using only the data for either the near or far side of the Moon yields almost identical most likely component fractions (rows 16 and 17), and the results for polar and equatorial regions in rows 18 and 19 are very similar too.

A significant difference is seen between the component fractions inferred from northern and south-

Table 1: Most likely parameter values calculated on a grid with spacing 0.005. Statistical uncertainties are of order 0.01 in all cases, which is smaller than the systematic variations arising from different subsets of the data, or model assumptions. The default model is for the ‘thorium-corrected’ input map. Lines 1-8 represent changes to the model, whereas lines 9-21 are for the default model with different subsets of the data.

Row number	Experiment	f_1	f_2	f_3
1	default	0.010	0.455	0.535
2	no HEE correction	0.020	0.450	0.530
3	no CR correction too	0.020	0.440	0.540
4	no thorium	0.005	0.460	0.535
5	epi/fast HEE template	0.010	0.465	0.525
6	coupled reconstructions	0.010	0.455	0.535
7	no pixion reconstructions	0.005	0.455	0.540
8	max $N_{\text{side}} = 128$	0.010	0.455	0.535
9	$0 < t/\text{days} < 90$	0.000	0.450	0.550
10	$90 < t/\text{days} < 250$	0.040	0.435	0.525
11	$250 < t/\text{days} < 335$	0.040	0.450	0.510
12	$335 < t/\text{days} < 456$	0.035	0.455	0.510
13	$a/\text{km} < 45$	0.005	0.445	0.550
14	$45 < a/\text{km} < 55$	0.020	0.450	0.530
15	$55 < a/\text{km}$	0.015	0.445	0.540
16	near side	0.010	0.460	0.530
17	far side	0.005	0.455	0.540
18	$ \text{latitude} > 60^\circ$	0.020	0.430	0.550
19	$ \text{latitude} < 60^\circ$	0.015	0.440	0.545
20	latitude > 0	0.040	0.415	0.545
21	latitude < 0	0.010	0.475	0.515

ern hemisphere data (rows 20-21), with the north preferring more collimated and less uncollimated lunar flux than the south. This presumably reflects residual inaccuracies in the HEE template. It is reassuring though that, while statistically significant, these systematic changes in the most likely component fractions are of a magnitude that is very small relative to the difference between the values inferred here and those of Mitrofanov et al. (2010b).

3.4. Comparison with previous studies

Breaking down the average ~ 3.6 counts per second (over the whole period used) to count rates in the various components, the results presented here suggest that on average, these comprise ~ 0.1 per second in collimated epithermals, ~ 1.6 in uncollimated lunar HEE, and ~ 1.9 per second in spacecraft generated counts. Taking into account the variable number of sensors active during the period, the collimated epithermal count rate is similar to the result of Lawrence et al. (2010). This is not surprising, because it is based on a simple geometrical argument that scales the flux from the omni-directional LP experiment to the solid angle subtended by the collimator.

In the supporting online material for their paper, Mitrofanov et al. (2010b) perform a similar calculation where they scale the count rate from the LEND SETN to estimate the collimated lunar flux reaching the CSETN. However, they neglect the contribution of the locally generated background to the SETN count rate and overestimate the beaming of lunar epithermal neutrons. Both of these factors will lead to an erroneously high anticipated collimated flux.

The neutron beaming can be assessed using the type of argument that led to eq. (2). In order to recover the beaming factor of ‘about 2’ asserted by Mitrofanov et al. (2010b), the neutrons would need to be beamed with $\alpha \sim 1.5$, in contrast to the $\alpha = 0.5$ measured from Monte Carlo neutron transport modelling of the lunar regolith (Lawrence et al. 2006). This factor of ‘about 2’ appears to be 50% larger than one would infer for $\alpha = 0.5$.

Without an accurate description of the LEND instrument and detailed modelling of neutron transport within the spacecraft, it is difficult to

quantify the extent of the locally-generated background. However, it should be noted that the SETN is placed next to a large piece of polyethylene, which is known to moderate and scatter neutrons very effectively (Elphic et al. 2008). This is the reason it is used as the outer part of the collimator. Thus it is implausible that there are not significant numbers of neutrons entering the SETN that come from this polyethylene, rendering any attempt to scale the SETN count rate to predict the CSETN count rate of little worth. Comparing the LEND SETN and LP epithermal maps in Figures 11 and 3 respectively, it is apparent that they look qualitatively different in a way that suggests the SETN has an extra HEE component that decreases the dip in the mare regions.

While the collimated flux found here is in agreement with that anticipated by Lawrence et al. (2010), there are approximately 20 times as many background lunar HEE neutrons than they predicted based on an incomplete knowledge of the detector geometry. This appears to be a result of Lawrence et al. (2010) having been too optimistic in their assumption as to how effective the collimator was. Specifically, Lawrence et al. (2010) assumed a ^{10}B density of $2.5\text{g}/\text{cm}^3$, while the true density was slightly less than $1\text{g}/\text{cm}^3$ (Mitrofanov et al. 2010a). In addition, Lawrence et al. (2010) assumed that except for the opening aperture, the collimating material completely enclosed the ^3He sensors. In contrast, the true LEND collimator has ‘holes’ that allow neutrons to enter the ^3He sensor through the back side of the collimator (Mitrofanov et al. 2010a). Both of these effects will significantly increase the true background compared to that estimated by Lawrence et al. (2010). Consequently, one should view their conclusions concerning the LEND CSETN signal-to-noise ratios as having been too favourable by a factor of $\sqrt{20} \sim 4$.

4. Conclusions

A comprehensive maximum likelihood analysis has been performed on the LEND CSETN data to determine the sources of the neutrons that it detects. The fraction of detected neutrons that are collimated lunar epithermal neutrons is under 0.05, with the most likely fraction being ~ 0.01 . $0.4 - 0.45$ are uncollimated lunar HEE neutrons,

and the remaining 0.5 – 0.55 are neutrons generated in LRO by direct cosmic ray strikes. The two lunar component fractions are almost the opposite of those asserted by Mitrofanov et al. (2010b), who favour the lunar flux being predominantly collimated. However, the data themselves are completely inconsistent with this interpretation, both using the full likelihood analysis and also from a simple inspection of the global SETN and CSETN maps. The conclusions drawn by Mitrofanov et al. (2010b) concerning hydrogen distributions should thus be viewed with skepticism.

Given that the LEND CSETN is effectively producing an uncollimated map of the lunar HEE neutrons, albeit with a small contamination from a LEE collimated component and a large, but spatially uniform spacecraft background, the experiment would more usefully be called the LEND Sensor for High Energy Epithermal Neutrons (SHEEN). One would expect that the HEE neutrons will be less beamed than the LEE ones, because they are typically created by more grazing-incidence cosmic rays. This, in combination with the 50 km orbit of LRO relative to 30 km for LP, counteracts the effect of the small fraction of collimated LEE neutrons, meaning that the effective FWHM for neutrons entering the LEND SHEEN is comparable with that of the LP omni-directional epithermal detector.

The best available map of the variation of the lunar HEE flux, determined in this study and shown in Fig. 14, differs from the input template for the lunar HEE component that was estimated from LP results. This implies that the LEND SHEEN data contain extra information that, in conjunction with Monte Carlo neutron transport simulations, can be used to construct a global map of the lunar hydrogen distribution (albeit at a broad spatial resolution like LP). An ambiguity in the inferred hydrogen abundance from LEE neutron measurements in non-polar regions (Maurice et al. 2004; Lawrence et al. 2006) will be absent from the HEE neutron case (Johnson et al. 2002). Specifically, HEE neutrons are, unlike LEE neutrons, unaffected by absorption (Lawrence et al. 2006), but are still sensitive to hydrogen variations (Genetay et al. 2003; Lawrence et al. 2011).

A global map of the hydrogen abundance would provide a valuable, new constraint on models for

the lunar water cycle at low latitudes and a useful consistency check of the high-altitude hydrogen maps from LP. With the recent infra-red measurements indicating the existence of surficial water at low latitudes and the LCROSS discovery of water in a small patch of the Cabeus crater near to the lunar south pole, a global hydrogen map would help to tie together these two separate strands of evidence concerning lunar water. This study has shown that data from the LEND experiment have the capacity to provide a global hydrogen map, at a resolution similar to that which LP achieved near to the poles. However, this conclusion relies upon a correct interpretation of the observational data and understanding of the instrumental capabilities. In order to exploit the full potential of the LEND SHEEN data with confidence, one would need a more detailed modelling of the detector response, with both position and energy, than is currently available.

The Bartol Research Institute neutron monitor program is supported by the United States National Science Foundation under grants ANT-0739620 and ANT-0838839, and by the University of Delaware Department of Physics and Astronomy and Bartol Research Institute. V. Eke acknowledges helpful discussions with C. Frenk and A. Jenkins. D. Lawrence acknowledges the support of the NASA Lunar Science Institute.

REFERENCES

- Arnold, J. R., 1979, *JGR*, 84, 5659
- Butler, B. J., 1997, *JGR*, 102, 19283
- Campbell, D. B., Campbell, B. A., Carter, L. M., Margot, J.-L., Stacy, N. J. S., 2006, *Nature*, 443, 835
- Chin, G. et al., 2007, *Space Sci. Rev.*, 129, 391
- Clark, R. N., 2009, *Science*, 326, 562
- Colaprete, A. et al., 2010, *Science*, 330, 463
- Crider, D. H., Vondrak, R. R., *JGR*, 105, 26773
- Eke, V. R., Teodoro, L. F. A., Elphic, R. C., 2009, *Icarus*, 200, 12

- Elphic, R. C., Lawrence, D. J., Feldman, W. C., Barraclough, B. L., Maurice, S., Binder, A. B., Lucey, P. G., 1998, *Science*, 281, 1493
- Elphic, R. C., Eke, V. R., Teodoro, L. F. A., Lawrence, D. J., Bussey, D. B. J., 2007, *GRL*, 34, L13204
- Elphic, R. C., Chu, P., Hahn, S., James, M. R., Lawrence, D. J., Prettyman, T. H., Johnson, J. B., Podgorney, R. K., 2008, *AsBio*, 8(3), 639
- Epstein, S., Taylor, H. P., Jr., 1973, *Proc. Lunar Sci. Conf.*, 4, 1559
- Fa, W., Wiczorek, M. A., Heggy, E., 2011, *JGR*, 116, 03005
- Feldman, W. C., Reedy, R. C., McKay, D. S., 1991, *GRL*, 18, 2157
- Feldman, W. C., Barraclough, B. L., Maurice, S., Elphic, R. C., Lawrence, D. J., Thomsen, D. R., Binder, A. B., 1998a, *Science*, 281, 1489
- Feldman, W. C., Maurice, S., Binder, A. B., Barraclough, B. L., Elphic, R. C., Lawrence, D. J., 1998b, *Science*, 281, 1496
- Feldman, W. C., Lawrence, D. J., Elphic, R. C., Barraclough, B. L., Maurice, S., Genetay, I., 2000, *JGR*, 105, 4175
- Feldman, W. C. et al., 2001, *JGR*, 106, 23231
- Gasnault, O., Feldman, W. C., Maurice, S., Genetay, I., d'Uston, C., Prettyman, T. H., Moore, K. R., 2001, *GRL*, 28, 3797
- Genetay, I., Maurice, S., Feldman, W. C., Gasnault, O., Lawrence, D. J., Elphic, R. C., d'Uston, C., Binder, A. B., 2003, *P&SS*, 51, 271
- Gorski, K. M., Hivon, E., Banday, A. J., Wandelt, B. D., Hansen, F. K., Reinecke, M., Bartelmann, M., 2005, *ApJ*, 622, 759
- Johnson, J. R., Feldman, W. C., Lawrence, D. J., Maurice, S., Swindle, T. D., Lucey, P. G., 2002, *JGR*, 107(E2), 5008
- Lawrence, D. J., Feldman, W. C., Barraclough, B. L., Binder, A. B., Elphic, R. C., Maurice, S., Thomsen, D. R., 1998, *Science*, 281, 1484
- Lawrence, D. J., Feldman, W. C., Elphic, R. C., Little, R. C., Prettyman, T. H., Maurice, S., Lucey, P. G., Binder, A. B., 2002, *JGR*, 107(E12), 5130
- Lawrence, D. J., Elphic, R. C., Feldman, W. C., Prettyman, T. H., Gasnault, O., Maurice, S., 2003, *JGR*, 108(E9), 5102
- Lawrence, D. J., Feldman, W. C., Elphic, R. C., Hagerty, J. J., Maurice, S., McKinney, G. W., Prettyman, T. H., 2006, *JGR (Planets)*, 111, E08001
- Lawrence, D. J., Elphic, R. C., Feldman, W. C., Funsten, H. O., Prettyman, T. H., 2010, *Astrobiology*, 10, 183
- Lawrence, D. J., Eke, V. R., Elphic, R. C., Feldman, W. C., Funsten, H. O., Prettyman, T. H., Teodoro, L. F. A., 2011, *Science*, 334, 1058
- Lawrence, D. J., 2011, *Nature Geoscience*, 4, 586
- Lingenfelter, R. E., Canfield, E. H., Hess, W. N., 1961, *JGR*, 66, 9
- Maurice, S., Lawrence, D. J., Feldman, W. C., Elphic, R. C., Gasnault, O., 2000, *JGR*, 105(E8), 20365
- Maurice, S., Lawrence, D. J., Feldman, W. C., Elphic, R. C., Gasnault, O., 2004, *JGR*, 109, E07S04
- McKinney, G. W., Lawrence, D. J., Prettyman, T. H., Elphic, R. C., Feldman, W. C., Haggerty, J. J., 2006, *JGR*, 111, E060004
- Metzger, A. E., Drake, D. M., 1990, *JGR*, 95, 449
- Mitrofanov, I. G. et al., 2008, *Astrobiology*, 8, 793
- Mitrofanov, I. G. et al., 2010a, *SSRv*, 150, 183
- Mitrofanov, I. G. et al., 2010b, *Science*, 330, 483
- Mitrofanov, I. G., Boynton, W. V., Litvak, M. L., Sanin, A. B., Starr, R. D., 2011, *Science*, 334, 1058
- Noda, H., Araki, H., Goossens, S., Ishihara, Y., Matsumoto, K., Tazawa, S., Kawano, N., Sasaki, S., 2008, *GRL*, 35, L24203

- Nozette, S., Lichtenberg, C. L., Spudis, P., Bonner, R., Ort, W., Malaret, E., Robinson, M., Shoemaker, E., 1996, *Science*, 274, 1495
- Pieters, C. M. et al., 2009, *Science*, 326, 568
- Schultz, P. H., Hermalyn, B., Colaprete, A., Ennico, K., Shirley, M., Marshall, W.S., 2010, *Science*, 330, 468
- Spudis, P. D. et al., 2010, *GRL*, 37, L06204
- Stacy, N. J. S., Campbell, D. B., Ford, P. G., 1997, *Science*, 276, 1527
- Sunshine, J. M., Farnham, T. L., Feaga, L. M., Groussin, O., Merlin, F., Milliken, R. E., A'Hearn, M. F., 2009, *Science*, 326, 565
- Teodoro, L. F. A., Eke, V. R., Elphic, R. C., 2010, *GRL*, 37, L12201

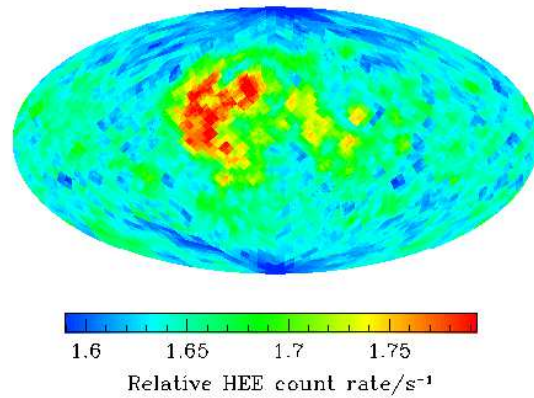


Fig. 14.— Mollweide projection of the final relative HEE count rate map from the LEND SHEEN data set using $N_{\text{side}} = 64$. The arbitrary normalisation is chosen to match the mean count rate from the HEE component over the first 456 days of lunar mapping. Note that the correction for the correlated residuals on scales of ~ 200 km is visible.